



Carnegie Supernova Project-II: A New Method to Photometrically Identify Sub-types of Extreme Type Ia Supernovae

C. Ashall¹, J. Lu¹, C. Burns², E. Y. Hsiao¹, M. Stritzinger³, N. B. Suntzeff⁴, M. Phillips⁵, E. Baron^{6,7}, C. Contreras⁵, S. Davis¹, L. Galbany⁸, P. Hoefflich¹, S. Holmbo³, N. Morrell⁵, E. Karamahmetoglu³, K. Krisciunas⁴, S. Kumar¹, M. Shahbandeh¹, and S. Uddin²

¹ Department of Physics, Florida State University, Tallahassee, FL 32306, USA; chris.ashall24@gmail.com

² Observatories of the Carnegie Institution for Science, 813 Santa Barbara Street, Pasadena, CA 91101, USA

³ Department of Physics and Astronomy, Aarhus University, Ny Munkegade 120, DK-8000 Aarhus C, Denmark

⁴ George P. and Cynthia Woods Mitchell Institute for Fundamental Physics & Astronomy, Texas A&M University, Department of Physics and Astronomy, 4242 TAMU, College Station, TX 77843, USA

⁵ Carnegie Observatories, Las Campanas Observatory, 601 Casilla, La Serena, Chile

⁶ Homer L. Dodge Department of Physics and Astronomy, University of Oklahoma, 440 West Brooks, Room 100, Norman, OK 73019-2061, USA

⁷ Hamburger Sternwarte, Gojenbergsweg 112, D-21029 Hamburg, Germany

⁸ Departamento de Física Teórica y del Cosmos, Universidad de Granada, E-18071 Granada, Spain

Received 2020 February 6; revised 2020 March 23; accepted 2020 March 24; published 2020 May 15

Abstract

We present a new method to photometrically delineate between various sub-types of Type Ia supernovae (SNe Ia). Using the color-stretch parameters, s_{BV} or s_{gr} , and the time of i -band primary maximum relative to the B -band (t_{\max}^{i-B}) or g -band (t_{\max}^{i-g}) maximum it is demonstrated that 2003fg-like, 1991bg-like, and 2002cx-like SNe Ia can be identified readily. In the cases of these extreme SNe Ia, their primary i -band maximum occurs after the time of the B - or g -band maxima. We suggest that the timing of the i -band maximum can reveal the physical state of the SN Ia explosion as it traces: (i) the speed of the recombination front of iron group elements in the ejecta, (ii) the temperature evolution and rate of adiabatic cooling in the ejecta and, (iii) the presence of interaction with a stellar envelope. This photometric sub-typing can be used in conjunction with other SNe analysis, such as the Branch diagram, to examine the physics and diversity of SNe Ia. The results here can also be used to screen out non-Ia SNe from cosmological samples that do not have complete spectroscopic typing. Finally, as future surveys like that of the Vera C. Rubin Observatory (previously referred to as the Large Synoptic Survey Telescope) create large databases of light curves of many objects this photometric identification can be used to readily identify and study the rates and bulk properties of peculiar SNe Ia.

Unified Astronomy Thesaurus concepts: Type Ia supernovae (1728); Supernovae (1668); Time domain astronomy (2109)

1. Introduction

Knowledge about Type Ia supernovae (SNe Ia) has revolutionized the study of an immense volume of the cosmos. To date they have been used to map out the expansion rate of the universe, providing the first observational evidence that it is accelerating (Riess et al. 1998; Perlmutter et al. 1999). SNe Ia also provide a measure of the local Hubble constant (e.g., Burns et al. 2018), constrain the dark energy equation-of-state parameter w (e.g., Scolnic et al. 2018), and have the potential to map out the local distribution of dark matter through peculiar velocity studies (Feindt et al. 2015). Currently the use of SNe Ia as standardizable candles is not limited by sample size, but a complex matrix of subtle systematic errors, where the lack of understanding of SNe Ia physics and diversity contributes a major fraction of the total error budget (Betoule et al. 2014).

We now recognize myriad varieties of SNe Ia. Maximum light spectra have been used to classify normal SNe Ia into four sub-groups: core-normal (CN), shallow silicon, cool, and broad line (Branch et al. 2006). There are also many sub-types of SNe Ia including (i) the luminous 1991T-like SNe (Filippenko et al. 1992b; Phillips et al. 1992), (ii) the sub-luminous 1991bg-like SNe (Filippenko et al. 1992a; Leibundgut et al. 1993), (iii) the broad but faint 2002cx-like SNe (Li et al. 2003; Foley et al. 2013; Jha 2017), (iv) the over-luminous and possibly “Super-

Chandrasekhar” mass SNe Ia, 2003fg-like SNe Ia (Howell et al. 2006; Hicken et al. 2007; Scalzo et al. 2010), (v) the 2002ic-like SNe Ia that show evidence of strong interaction with their circumstellar medium (Hamuy et al. 2003), (vi) and the 2006bt-like SNe Ia, which have broad, slowly declining light curves but lack a prominent secondary maximum in the i -band (Foley et al. 2010). Identifying the differences and diversity of SNe Ia is key if we are to improve upon their effectiveness as a multi-purpose cosmological tool and understand their diversity and progenitor scenarios.

Commonly, SNe Ia are classified using maximum light spectra. However, with just one spectrum it is often not possible to firmly identify to which sub-type of SNe Ia the object belongs. Furthermore, spectra require significant exposure times, and it is not possible to obtain spectra of all transients. Current and future surveys, such as the Zwicky Transient Facility (ZTF) and the Vera C. Rubin Observatory (previously referred to as the Large Synoptic Survey Telescope (LSST)), scan the night sky with a daily cadence, and obtain light curves of many more supernovae than can be followed spectroscopically with current infrastructure.

Previous work has used the SNe Ia light curve fitter SiFTO in an attempt to distinguish between SNe Ia sub-classes (González-Gaitán et al. 2014). Here we used multi-band light curve observations from the Carnegie Supernova Project I and II (CSP I and CSP II) to present a new way to identify rare

supernovae (SNe) that likely have a thermonuclear origin. We use direct observational parameters and concentrate on the *i*-band as it shows the largest diversity among SNe Ia.

2. Observational Sample

The CSP I and II obtained an unprecedented sample of over 300 SNe Ia light curves on a stable and well-measured photometric system (Contreras et al. 2010; Stritzinger et al. 2011; Krisciunas et al. 2017; Hsiao et al. 2019; Phillips et al. 2019). Here, we consider a subset of these objects characterized by high-cadence *B*-, *V*-, *g*-, and *i*-band light curve coverage. Photometric data from the CSP were obtained with the Swope telescope at Las Campanas Observatory, and reduced, calibrated, and template-subtracted following the procedures described in Krisciunas et al. (2017) and Phillips et al. (2019). Definitive light curve photometry from the CSP I was published by Krisciunas et al. (2017) and those from CSP II will be published in the near future (N. B. Suntzeff et al. 2020, in preparation).

The selection criteria for building the sub-sample examined in this work include: pre-maximum *BVi*-band photometry, a clearly discernible time of maximum light, and photometric coverage extending through 30 days past maximum. The normal SNe have an error on the time of maximum ($t_{\max}[\text{err}]$) less than 0.5 day, other SNe have $t_{\max}[\text{err}] < 0.6$ day, except for the 03fg-like objects, which have a $t_{\max}[\text{err}] < 2.5$ days. A larger error budget was set for the peculiar SNe to ensure that the sample sizes were large enough.

Following these requirements when using the *B*-band we identify: 103 normal SNe Ia, four 1991T-like, six 03fg-like, 11 1991bg-like, five 2002cx-like, and two 2006bt-like SNe. When using the *g*-band instead of the *B*-band the sample size is smaller. There are 60 normal, zero 1991T-like, 10 1991bg-like, three 2003fg-like, and five 2002cx-like SNe. Additionally, in both samples we have added three more 2003fg-like SNe Ia from the literature, which are SNe 2006gz (Hicken et al. 2007), 2012dn (Taubenberger et al. 2019), and ASASSN-15pz (Chen et al. 2019). All of the objects in the sample were spectroscopically classified to determine their sub-type.

We have corrected the SNe for Galactic extinction using values from Schlafly & Finkbeiner (2011), but not for host-galaxy extinction. The average redshift of the SNe in the sample is 0.03 ± 0.02 . Therefore, we have not performed *K*-corrections because all of our objects are low redshift (less than 0.1), therefore the effect on the time of maximum will be minimal. It is also non-trivial to compute *K*-corrections for peculiar SNe Ia sub-types until more spectra are available. However, the three non-CSP 03fg-like SNe were *S*-corrected to the natural CSP system, using the spectra of SN 2009dc. Finally, all of the light curves were converted to rest frame by scaling the number of days since maximum by $\frac{1}{(1+z)}$.

The parameters used in this analysis are the time of *i*-band maximum relative to *B* or *g* maximum (t_{\max}^{i-B} , t_{\max}^{i-g}) and the color-stretch parameters s_{BV} and s_{gr} (Burns et al. 2014). The color-stretch parameter, s_{BV} , is dimensionless and defined as the time difference between *B*-band maximum and the reddest point in the post-maximum *B* – *V* color curve divided by 30 days, where typical SNe Ia have $s_{BV} \approx 1$. The s_{BV} values of the SNe were obtained from Gaussian Processes interpolation to the light curves. The Gaussian Processes interpolation accounts for uncertainties through its covariance function. As recent surveys are often limited to Sloan (*ugriz*) filters, and lack

the more extensive information obtained with the traditional Johnson (*BV*) filters, we use a new parameter s_{gr} . s_{gr} corresponds to the time of (*g* – *r*) maximum relative to *g*-band maximum, normalized by 30 days. s_{gr} is fitted using the same approach as s_{BV} . Using 79 SNe Ia, we find a precise linear correlation between s_{gr} and s_{BV} . The correlation is represented by

$$s_{gr} = 1.03(01) + 0.93(02) * (s_{BV} - 1), \quad (1)$$

with an rms = 0.05; see the left panel of Figure 1. s_{gr} contains the similar information as s_{BV} . This is demonstrated in the right-hand panel of Figure 1 where there is a strong correlation between M_B and s_{gr} . This is similar to the trend seen between M_B and s_{BV} in Burns et al. (2018). We find that a two-piece linear function fits the data best with a break at 0.71. The data were fit using the PYTHON package PWLF, where a global optimization algorithm was used to determine the best break point location by solving least squares fits. The best fit equations are given by

$$M_B = \begin{cases} -19.00 - 1.29(s_{gr} - 0.71) & \text{if } s_{gr} > 0.71 \\ -19.00 - 5.51(s_{gr} - 0.71) & \text{if } s_{gr} < 0.71. \end{cases} \quad (2)$$

To determine t_{\max}^{i-B} and t_{\max}^{i-g} , the *B*-, *g*-, and *i*-band light curves were fit with Gaussian processes, where the errors are once again accounted for in the covariance function. The fitting process was performed using the Gaussian processes function in SNooPy (Burns et al. 2011). The SNe data were directly fit. No templates were used in the fitting procedure as they are not available for the extreme SNe Ia, and using normal SNe Ia templates would bias the values obtained.

3. Maximum Light Spectra

SNe Ia are dominated by line opacity. Where the elements, their abundances, and their ionization state are determines the optical display. Understanding which lines are present in each sub-type can provide clues about the diversity that is seen in the light curves. Hence, in this section we discuss the differences in the maximum light spectra for each sub-type.

The maximum light spectra of all SNe Ia are dominated by intermediate-mass and iron group elements and lack H and He features. All of the spectra prominently display the iconic Si II $\lambda 6355$ feature. Therefore, they all belong to the SNe Ia category and originate from the thermonuclear explosion of a white dwarf. All the various sub-types follow those commonalities, and each spectrum has its own peculiarities that set it apart from a CN (Branch et al. 2006) SN Ia. Below we discuss some of the differences.

At maximum light a normal SNe Ia spectrum mainly displays doubly and singly ionized species. Specifically; Ca II $\lambda 3968$, 3933, Si II $\lambda 4130$, Mg II $\lambda 4481$, Si III $\lambda 4552$, Fe II $\lambda 5196$, Fe III $\lambda 5156$, S II $\lambda 5453 + \lambda 5606$, Si II $\lambda 5978$ 6355, O I $\lambda 7771$, and Ca II $\lambda 8498$, 8542, 8662 (e.g., Branch et al. 2006; Ashall et al. 2018).

1991T-like SNe are brighter and hotter than normal SNe Ia, with features associated with doubly ionized Fe III and Si III. Due to this higher temperature 1991T-like SNe have a weak Si II $\lambda 6355$ feature. This high ionization state has been suggested to be caused by a large amount of ^{56}Ni in ejecta and heating of the photosphere (Filippenko et al. 1992b; Phillips et al. 1992; Sasdelli et al. 2014).

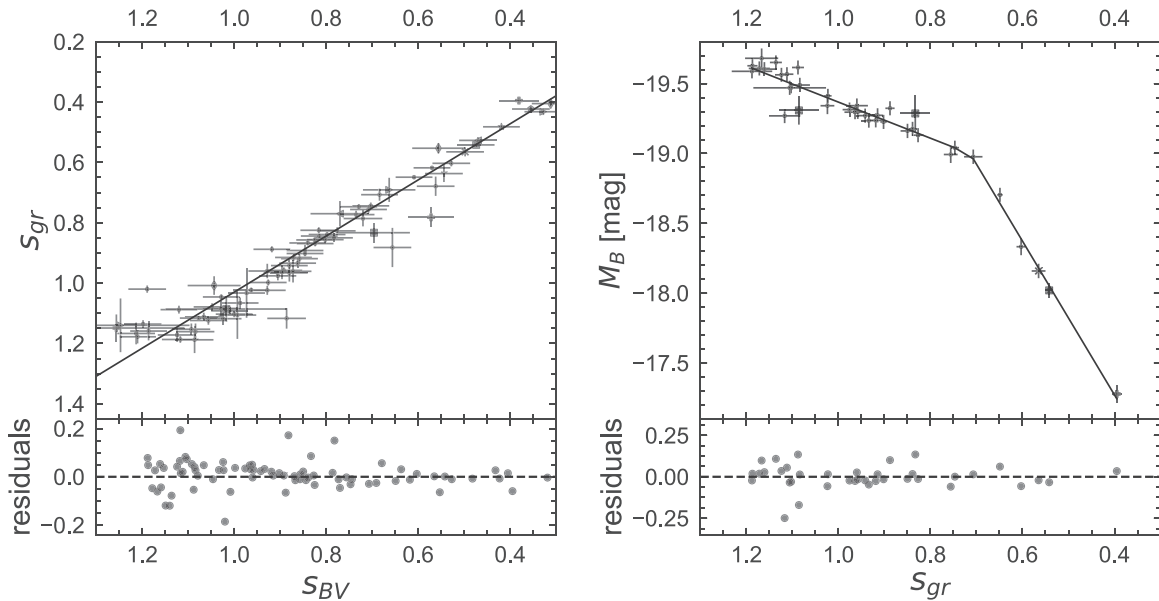


Figure 1. Left panel: s_{BV} vs. s_{gr} produced using 79 SNe Ia from the CSP I and II. Right panel: M_B vs. s_{gr} for a sample of 38 SNe Ia which have M_B values from Burns et al. (2018).

SN 2003fg-like SNe are events that are as bright, and usually brighter, than normal SNe Ia. However, the ionization state of these SNe is much lower than that of a 1991T-like. They look remarkably like normal SNe Ia, with the exception that they exhibit weak Ca II features (Scalzo et al. 2010). They also have two strong C II features at $\lambda 6580$ and $\lambda 7234$, which points to a large amount of unburnt material in the ejecta (Howell et al. 2006; Hicken et al. 2007). Hachinger et al. (2012) demonstrated that the ionization state of the ejecta does not correspond to the luminosity of these events, and concluded that there must be some additional source of energy, for example interaction with H/He deficient material, such as a stellar envelope.

2002cx-like are dominated by doubly ionized species, such as Fe III, similar to that of 1991T-like events (Li et al. 2003; Phillips et al. 2007; Foley et al. 2013). They are much less luminous and have low expansion velocities ranging from ~ 2000 – 7000 km s^{-1} (Jha 2017).

Finally, the spectra of 1991bg-like SNe are dominated by singly ionized species, a large Si II line ratio, a strong O I feature, and the appearance of a Ti II feature at 4400 \AA (Filippenko et al. 1992a; Leibundgut et al. 1993). It has been suggested that this is due to a temperature evolution from normal to 1991bg-like SNe Ia, where the less luminous SNe have less ^{56}Ni , less heating, and therefore a lower ionization state (Nugent et al. 1995).

4. Results

4.1. Thermonuclear SNe

In Figure 2 we present the B -, g -, and i -band light curves of the SNe in our sample separated by sub-type, normalized in both flux and the time of the B -band maximum. All of the normal SNe Ia exhibit a secondary i -band maximum and the time of the primary i -band maximum (-2.25 ± 0.91 days) occurs prior to the epoch of B -band maximum. In the B -band, 1991T-like SNe show a similar trend to the normal SNe Ia, but they tend to be broader than the normal SNe Ia population.

They also have a prominent secondary i -band maximum, and a primary i -band maximum (-1.12 ± 0.47 days) that peaks before the B -band maximum. However, there is need of more 1991T-like high-cadence light curves to determine the significant of this behavior.

The 2003fg-like SNe Ia may have longer rise times than normal SNe Ia and on average, they also have broader B -band light curves. In the i -band they differ significantly from normal objects. Their light curves are very broad and have a weak or no secondary maximum. Furthermore, the primary i -band maximum (2.98 ± 2.10 d) occurs after the time of B -band maximum.

The 1991bg-like SNe have B -band light curves that decline faster than normal SNe Ia. In the i -band they also differ from normal SNe Ia in that their primary maximum (2.51 ± 1.61 days) occurs after the time of B -band maximum. In the B -band, 2002cx-like SNe also decline rapidly, but less so than 1991bg-like SNe. In the i -band 2002cx-like SNe peak significantly later (9.17 ± 1.85 days) compared to all other sub-types. Both 1991bg-like and 2002cx-like SNe do not exhibit a prominent i -band secondary maxima.

Similar trends are seen in the timing of i -band maximum relative to g -band maximum. For normal and 1991T-like SNe, the timing of the i -band primary maximum is before that of the g -band maximum, and for 1991bg-like, 2002cx-like, and 2003fg-like SNe Ia the i -band maximum is after that of the g -band maximum.

The i -band secondary maximum is thought to be produced when the photospheric radius reaches its maximum, after which a recombination front of iron group elements recedes through the ejecta (Höflich et al. 2002; Kasen 2006; Jack et al. 2015). For normal SNe the opacity drop starts at about +20 days, therefore they have a clear secondary i -band maximum. This timing of the secondary i -band maximum is a function of luminosity; brighter SNe Ia have a later secondary i -band maximum and later recombination of iron group elements due to increased opacity from higher temperatures and larger ^{56}Ni masses synthesized in the explosion. For 1991bg-like SNe, less

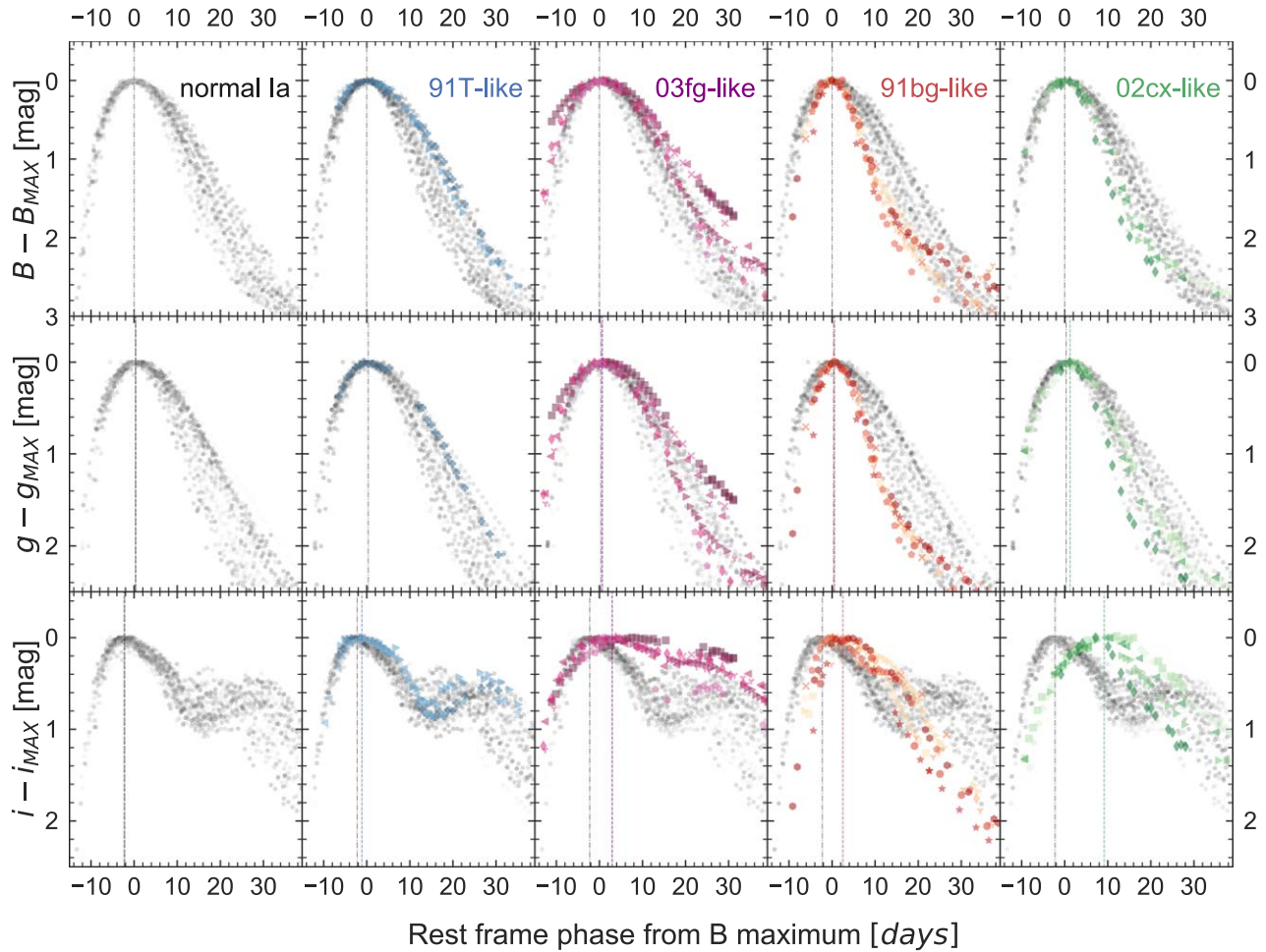


Figure 2. *B*-band (top panels) *g*-band (middle panels), and *i*-band (bottom panels) light curves for the SNe Ia sub-types. For all of the panels the normal SNe Ia are plotted in gray for comparison. For all of the panels the vertical gray dashed lines mark the mean time of maximum of the normal Ia population. For the middle and lower panels the dashed colored lines mark the mean time of the *g*-band (middle panels) or primary *i*-band (bottom panels) maximum for the corresponding sub-types.

luminosity implies less heating and an earlier drop in the opacities. The opacity drop starts at maximum light and leads to the merging of the first and secondary *i*-band maxima. Hence, 1991bg-like SNe all have $t_{\max}^{i-B} > 0$.

The 2003fg-like SNe have $t_{\max}^{i-B} > 0$, and ionization states similar or lower than normal SNe Ia. Generally, they also show expansion velocities that are low at maximum light. For example, the velocity of the Si II $\lambda 6355$ feature was $\sim 7500 \text{ km s}^{-1}$ at maximum light for SN 2009dc (Taubenberger et al. 2011). These objects do not show the *H*-band break in the near-infrared (NIR) spectra at +10 d, which occurs when the photosphere reaches the ^{56}Ni rich region (Hoeflich & Khokhlov 1996; Wheeler et al. 1998; Hsiao et al. 2015; Ashall et al. 2019a, 2019b). The variety of *H*-band break for different sub-types of SNe Ia can be seen in Figure 6 from Hsiao et al. (2019). All of this may be an indication that these objects have a large mass of carbon, oxygen, or intermediate-mass elements above the ^{56}Ni layers. This envelope can effectively trap the gamma-rays produced from the ^{56}Ni , leading to longer diffusion timescales and the recombination of iron group elements in the ejecta occurring over longer timescales.

The 2002cx-like SNe have high ionization states but *i*-band light curves that peak significantly later than normal SNe Ia. 2002cx-like SNe have the lowest expansion velocities of all the SNe Ia, in the range of $2000\text{--}7000 \text{ km s}^{-1}$, which may cause them to stay hot and highly ionized for a long time. It has been suggested that 2002cx-like SNe Ia come from a Chandrasekhar-mass white dwarf progenitor that experiences a pulsational delayed detonation (Stritzinger et al. 2015). In this scenario the photosphere recedes through the ejecta quickly and only keeps the material just above the photosphere highly ionized. This produces the narrow lines, high ionization, and lack of recombination of iron group elements leading to one *i*-band maximum. Alternatively, it has been suggested that 2002cx-like SNe come from the partial deflagration of a white dwarf, where the ejecta is fully mixed. In this scenario the ^{56}Ni in the outer layers produces the high ionization and a lack of recombination of iron group elements (Jha 2017). Generally, the low expansion velocities, high ionization state, and broad light curves of these objects suggest that they have the longest diffusion timescales, which produces a slow temperature evolution and adiabatic cooling and is the cause of the large t_{\max}^{i-B} .

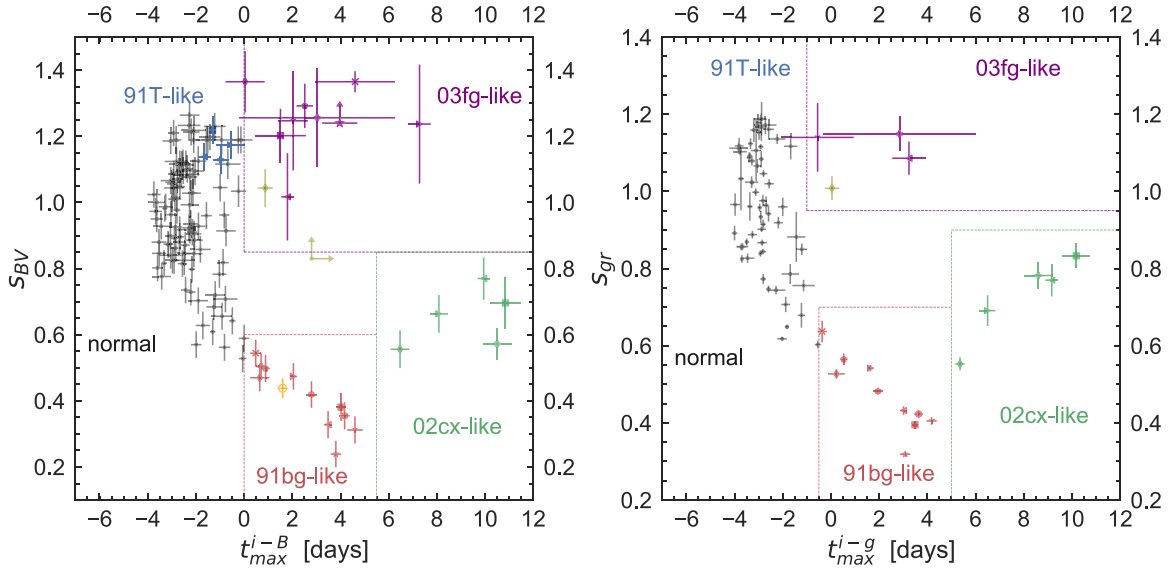


Figure 3. Color stretch parameter as a function of i -band maximum. Left panel: using s_{BV} and t_{\max}^{i-B} there is a clear separation between sub-types. Right panel: using s_{gr} and t_{\max}^{i-g} the separation is also seen but the sample size is smaller. The mean values of the sample and parameters for the grouping can be found in Table 1. In the left panel SN 2006bt (yellow diamond) and upper limits for SN 2006ot (yellow circle) are also plotted. SN 2006ot is a 2006bt-like SNe. For comparison we have also added SN 2016hbk (open orange circle) from Galbany et al. (2019) in the left panel.

Table 1
Average Values of s_{BV} , s_{gr} , t_{\max}^{i-B} , t_{\max}^{i-g} and the Parameters Used to Classify the Objects in Figure 3

Sub-type	Mean(s_{BV})	Mean(s_{gr})	Mean(t_{\max}^{i-B})	Mean(t_{\max}^{i-g})	Classification (B)	Classification (g)
Normal	0.95 ± 0.17	0.96 ± 0.16	-2.25 ± 0.91	-2.81 ± 0.76	$t_{\max}^{i-B} < 0$ and $s_{BV} > 0.5$	$t_{\max}^{i-g} < -0.5$ and $s_{gr} > 0.6$
91T-like	1.17 ± 0.04	...	-1.12 ± 0.47	...	$t_{\max}^{i-B} < 0$ and $s_{BV} > 1.1$...
03fg-like	1.25 ± 0.10	1.13 ± 0.03	2.98 ± 2.10	1.84 ± 2.09	$t_{\max}^{i-B} > 0$ and $s_{BV} > 0.85$	$t_{\max}^{i-g} > -1$ and $s_{gr} > 0.95$
91bg-like	0.41 ± 0.10	0.47 ± 0.10	2.51 ± 1.61	2.14 ± 1.59	$0 < t_{\max}^{i-B} < 5.5$ and $s_{BV} < 0.6$	$-0.5 < t_{\max}^{i-g} < 5.0$ and $s_{gr} < 0.7$
02cx-like	0.65 ± 0.09	0.73 ± 0.11	9.17 ± 1.85	7.96 ± 1.98	$t_{\max}^{i-B} > 5.5$ and $s_{BV} < 0.85$	$t_{\max}^{i-g} > 5.0$ and $s_{gr} < 0.9$

The color-stretch parameter, s_{BV} , has successfully been used in conjunction with other observables to distinguish SNe Ia properties (Ashall et al. 2018; Burns et al. 2018). Figure 3 shows s_{BV} and s_{gr} as a function of t_{\max}^{i-B} or t_{\max}^{i-g} . All of the extreme SNe, except 1991T-like, are classified by having $t_{\max}^{i-B} > 0$ day. They are also all located in distinct areas of this diagram.⁹ Table 1 contains the parameters that can be used to identify these groups.

The 1991bg-like, 2003fg-like, and 2002cx-like SNe are separated from the normal population, which points to different origins of these sub-classes. It is worth addressing whether there is a continuous distribution between most of the SNe Ia sub-types. For example, previous work has shown 1991bg-like SNe and normal SNe Ia come from a continuous distribution (Ashall et al. 2018; Burns et al. 2018). This is also seen in Figure 3, where 1991bg-like SNe are located at the end of the distribution of normal SNe Ia. In fact, it could be argued that the division between 1991bg-like and normal SNe Ia is slightly arbitrary and purely determined by the presence of Ti II and the ionization state seen in maximum light spectra. SN 2003fg-like objects are often thought to be their own distinct sub-type, and from Figure 3 this appears to be true. The peculiar SN 2006bt has been suggested to

be a connection between 2003fg-like SNe and normal SNe Ia (Foley et al. 2010), and its location in Figure 3 fits with this conclusion. Finally, it seems that the 2002cx-like SNe are a distinct group, and possibly come from a totally different origin.

4.2. Core-collapse SNe

The aim of this work is to produce a photometric sub-typing of SNe Ia, similar to that found with maximum light spectra in Branch et al. (2006). However, it is also interesting to understand where core-collapse SNe are located in this parameter space, and to see if their location offers insights on the physics of the Ia sub-groups. SNe II evolve over longer timescales than SNe Ia. For example SN 2012aw, a type II-SN, did not peak in $B - V$ until 90 days past B -band maximum, which would give it an s_{BV} of 3. The type II-L SN 2013ej peaked in the i -band at least 15 days after B -band maximum. This places SNe II outside of both axes of Figure 3. We also examined a type IIb (SN 1993J, Schmidt et al. 1993) which has s_{BV} of 0.9 and $t_{\max}^{i-B} \approx 3$, a Type Ib (SN 2009jf Valenti et al. 2011), which has $s_{BV} \approx 0.91$ and $t_{\max}^{i-B} \approx 8$, and a Type Ic (SN 2016coi; Prentice et al. 2018), that has $s_{BV} \approx 0.59$ and $t_{\max}^{i-B} \approx 7$. This places the Type IIb and Ib in the 2003fg-like area of Figure 3, and the Type Ic SN in the 2002cx-like area of the Figure 3.

⁹ It should be noted that this separation does not exist if using s_{gr} and the time of g -band maximum relative to r -band maximum.

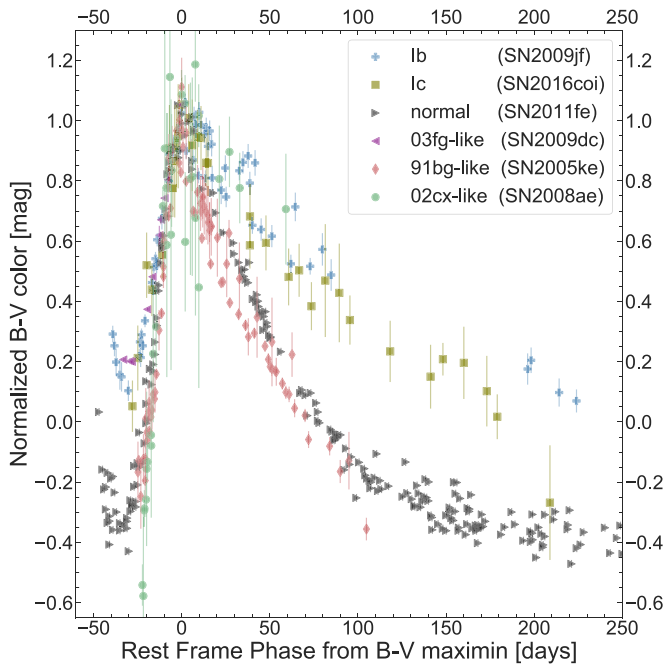


Figure 4. $B - V$ color curves of thermonuclear and core-collapse SNe as a function of time from $B - V$ maximum, normalized in both time and magnitude. The normal Ia, 1991bg-like SNe and 2002cx-like shown here all have a faster evolution after the time of $B - V$ maximum, whereas the core-collapse SNe and 2003fg-like SNe have a slower evolution.

Some additional information that could lead to clues about the SNe Ia sub-types is the gradient of the $B - V$ or $g - r$ color curve after the color turnover. For normal, 1991bg-like, and some 2002cx-like SNe (e.g., SN 2008ae), the slope after the $B - V$ maximum is much steeper than for core collapse SNe. For example, it takes SN 2011fe 80 days to change by one magnitude, whereas it takes 150 days for the type Ic SN 2016coi to change by the same amount; see Figure 4. However, the gradients of the color curves of core-collapse SNe and 2003fg-like SNe are similar.¹⁰ This may indicate that the photosphere is moving through ejecta with similar composition, probably a large carbon/oxygen-rich layer. For the 2003fg-like SNe the interaction with this large H/He deficient envelope could also be the cause of the excess luminosity compared to normal SNe Ia (Hachinger et al. 2012).

Although not the aim of this work, the results here may also be used alongside absolute magnitude to photometrically classify transient sources. For example, most stripped-envelope supernovae reach peak B -band absolute magnitudes of $M_B \approx -17$ to -18 (see Taddia et al. 2018, their Figure 8). However, even the faintest 2003fg-like SNe from the CSP sample and the literature peak at -19.3 mag (Taubenberger et al. 2019), making 2003fg-like events consistently at least one magnitude more luminous. Therefore, a cutoff of $M_B = -18.5$ mag could be used to separate core-collapse and 2003fg-like events. It should be noted that a larger sample of core-collapse SNe needs to be examined to test the validity of these results. Also, further data of extreme SNe Ia will enable the robustness of this method to be determined.

5. Conclusions

We present a new method to photometrically distinguish between sub-types of thermonuclear SNe. A set of B -, g -, and i -band light curves of 103 normal SNe Ia, four 1991T-like, nine 2003fg-like, 11 1991bg-like, five 2002cx-like SNe, and two 2006bt-like SNe have been used to demonstrate how the timing of the primary i -band maximum provides a clear means to discriminate between SN sub-types.

The peculiar 2003fg-like, 1991bg-like, and 2002cx-like SNe have their primary peak in the i -band later than that of the B -band and g -band. These sub-types also have a weak or no secondary i -band maximum. Using the time of primary i -band maximum in conjunction with the color-stretch parameters, s_{BV} or s_{gr} , it was found that normal, 2003fg-like, 1991bg-like, and 2002cx-like SNe fall into distinct photometric groups that correspond to their spectral classification.

We speculate that the timing of the i -band maximum is potentially caused by multiple factors: (i) 1991bg-like SNe have low ^{56}Ni masses, low ionization, and an early onset of the recombination front, which merges the two i -band maxima normally seen in SNe Ia, (ii) 2003fg-like SNe have a lack of secondary i -band maximum that may be due to long diffusion timescales, caused by a large optically thick envelope around the ^{56}Ni region, (iii) and 2002cx-like SNe have a high ionization state, lack of recombination of iron group elements, and low expansion velocities, all of which produce a slow temperature evolution and an ejecta that slowly adiabatically cools. This may cause a lack of secondary i -band maximum, and a later primary maximum.

Future surveys, such as LSST, will produce massive databases of high-cadence light curves of SNe, and using the identification scheme presented here it will be possible to unambiguously identify the SNe Ia sub-type where there is poor, uncertain, or no spectral classification. The results here can also be used in conjunction with already existing spectral classifications, such as those from Branch et al. (2006) to further refine our understanding of SNe Ia physics. This work can also be used as a guide line to screen out non-Ia SNe from cosmological samples that do not have complete spectroscopic typing. Finally, as more sub-types of thermonuclear SNe are discovered, high-cadence i -band data can be used to determine their connection with the existing sub-types.

M.S. is supported in part by a generous grant (13261) from VILLUM FONDEN. E.B. acknowledges support from NASA grant NNX16AB25G. N.B.S. acknowledges support from the Texas A&M University Mitchell/Heep/Munnerlyn Chair in Observational Astronomy. L.G. was funded by the European Union's Horizon 2020 research and innovation programme under the Marie Skłodowska-Curie grant agreement No. 839090. The CSP II has been funded by the NSF under grants AST-0306969, AST-0607438, AST-1008343, AST-1613426, AST-1613455, and AST-1613472, and in part by a Sapere Aude Level 2 grant funded by the Danish Agency for Science and Technology and Innovation (PI: M.S.).

Facilities: du Pont, Swope, Python, IRAF, IDL.

Appendix Table

Table A1 contains the parameters derived from light curves of the SNe.

¹⁰ It should be noted that the gradient of the color curve is also sensitive to the total-to-selective extinction (R_V).

Table A1
Table of SNe Parameters

SN Name	Redshift	t_{\max}^B (MJD)	t_{\max}^{i-B} (days)	t_{\max}^{i-g} (days)	S_{BV}	S_{gr}	SN Type
SN2006bt	0.032	53857.77 \pm 0.21	0.87 \pm 0.31	0.04 \pm 0.30	1.04 \pm 0.06	1.01 \pm 0.03	06bt-like
SN2006ot	0.053	54065.68 \downarrow	2.8 \uparrow	...	0.83 \uparrow	...	06bt-like
ASAS14kd	0.024	56981.76 \pm 0.21	-0.98 \pm 0.33	...	1.13 \pm 0.04	...	91T-like
SN2014dl	0.033	56934.65 \pm 0.09	-1.31 \pm 0.14	...	1.22 \pm 0.04	...	91T-like
SN2014eg	0.019	56991.26 \pm 0.47	-0.56 \pm 0.58	...	1.17 \pm 0.04	...	91T-like
LSQ12gdj	0.030	56252.17 \pm 0.25	-1.65 \pm 0.27	...	1.14 \pm 0.04	...	91T-like
SN2007if	0.074	54348.18 \pm 2.55	3.03 \pm 3.24	2.85 \pm 3.14	1.26 \pm 0.15	1.15 \pm 0.05	03fg-like
LSQ14fmg	0.066	56938.71 \pm 0.58	1.51 \pm 1.05	...	1.20 \pm 0.08	...	03fg-like
ASASSN-15hy	0.019	57150.67 \pm 0.33	7.28 \pm 0.47	5.97 \pm 0.65	1.24 \pm 0.18	...	03fg-like
SN2013ao	0.044	56362.11 \pm 0.11	1.80 \pm 0.26	3.24 \pm 0.69	1.02 \pm 0.13	1.09 \pm 0.04	03fg-like
MLS140102 ^a	0.077	56667.36 \pm 0.31	3.97 \pm 0.73	...	1.24 ^b	...	03fg-like
ASASSN-15pz	0.000	57306.65 \pm 0.76	0.04 \pm 0.81	...	1.37 \pm 0.09	...	03fg-like
SN2012dn	0.010	56132.59 \pm 0.59	2.04 \pm 0.61	-0.55 \pm 1.50	1.25 \pm 0.15	1.14 \pm 0.09	03fg-like
SN2006gz	0.024	54019.97 \pm 0.30	4.60 \pm 1.65	...	1.37 \pm 0.03	...	03fg-like
SN2009dc	0.021	54946.94 \pm 0.21	2.52 \pm 0.34	1.91 \pm 0.49	1.29 \pm 0.07	...	03fg-like
SN2012Z	0.007	55967.22 \pm 0.23	10.50 \pm 0.60	8.60 \pm 0.60	0.57 \pm 0.05	0.78 \pm 0.03	02cx-like
PTF14ans	0.032	56781.76 \pm 0.31	10.85 \pm 0.65	10.18 \pm 0.58	0.70 \pm 0.08	0.83 \pm 0.03	02cx-like
SN2014ek	0.023	56957.39 \pm 0.25	8.08 \pm 0.37	6.50 \pm 0.32	0.66 \pm 0.06	0.69 \pm 0.04	02cx-like
SN2005hk	0.013	53684.62 \pm 0.12	9.94 \pm 0.25	9.16 \pm 0.26	0.77 \pm 0.06	0.77 \pm 0.04	02cx-like
SN2008ha	0.005	54781.89 \pm 0.37	6.47 \pm 0.39	5.36 \pm 0.19	0.56 \pm 0.06	0.55 \pm 0.02	02cx-like
LSQ14ip	0.061	56688.06 \pm 0.150	0.71 \pm 0.214	...	0.50 \pm 0.041	...	91bg-like
KISS15m	0.024	57143.68 \pm 0.180	4.02 \pm 0.211	3.49 \pm 0.121	0.38 \pm 0.042	0.40 \pm 0.010	91bg-like
SN2016hmk	0.016	57689.48 \pm 3.27	1.60 \pm 0.20	...	0.44 \pm 0.03	...	16hmk
SN2015bo	0.016	57075.76 \pm 0.110	2.05 \pm 0.140	1.64 \pm 0.093	0.47 \pm 0.040	0.54 \pm 0.008	91bg-like
SN2009F	0.013	54841.80 \pm 0.110	3.48 \pm 0.176	3.01 \pm 0.140	0.33 \pm 0.041	0.43 \pm 0.011	91bg-like
SN2008bt	0.015	54571.98 \pm 0.200	0.65 \pm 0.397	0.23 \pm 0.347	0.47 \pm 0.041	0.53 \pm 0.011	91bg-like
SN2007N	0.013	54123.46 \pm 0.250	4.60 \pm 0.322	4.18 \pm 0.213	0.31 \pm 0.041	0.41 \pm 0.010	91bg-like
SN2007ba	0.039	54196.67 \pm 0.130	0.48 \pm 0.230	-0.37 \pm 0.195	0.54 \pm 0.041	0.64 \pm 0.028	91bg-like
LSQ11pn	0.033	55929.07 \pm 0.090	0.89 \pm 0.178	0.53 \pm 0.158	0.50 \pm 0.041	0.57 \pm 0.015	91bg-like
SN2007ax	0.007	54187.75 \pm 0.110	4.17 \pm 0.210	3.63 \pm 0.180	0.36 \pm 0.041	0.42 \pm 0.011	91bg-like
SN2006mr	0.006	54050.54 \pm 0.060	3.81 \pm 0.217	3.08 \pm 0.210	0.24 \pm 0.040	0.32 \pm 0.007	91bg-like
SN2005ke	0.005	53698.39 \pm 0.080	2.80 \pm 0.205	1.95 \pm 0.190	0.42 \pm 0.040	0.48 \pm 0.007	91bg-like
LSQ15alq	0.047	57154.13 \pm 0.20	-2.15 \pm 0.22	...	0.91 \pm 0.04	...	normal
PS1-14rx	0.067	56736.32 \pm 0.29	-2.48 \pm 0.43	...	0.83 \pm 0.04	...	normal
PTF11pbbp	0.029	55871.42 \pm 0.18	-2.09 \pm 0.23	...	1.19 \pm 0.04	...	normal
PTF13anh	0.062	56413.56 \pm 0.16	-1.56 \pm 0.23	...	0.96 \pm 0.04	...	normal
PTF13duj	0.017	56601.23 \pm 0.19	-0.93 \pm 0.31	...	1.19 \pm 0.04	...	normal
PTF13ebh	0.013	56622.90 \pm 0.08	-1.30 \pm 0.11	-1.83 \pm 0.09	0.61 \pm 0.04	0.65 \pm 0.01	normal
PTF13efe	0.075	56640.64 \pm 0.31	-1.22 \pm 0.46	...	1.23 \pm 0.04	...	normal
PTF14aaf	0.059	56739.46 \pm 0.43	-0.13 \pm 0.49	...	1.19 \pm 0.04	...	normal
PTF14aje	0.028	56757.99 \pm 0.27	-1.26 \pm 0.31	-1.88 \pm 0.18	0.68 \pm 0.04	0.71 \pm 0.02	normal
PTF14fpg	0.034	56930.56 \pm 0.27	-2.20 \pm 0.35	-2.89 \pm 0.24	1.21 \pm 0.04	1.17 \pm 0.04	normal
LSQ14xi	0.051	56719.97 \pm 0.31	-2.04 \pm 0.37	...	1.10 \pm 0.04	...	normal
LSQ14wp	0.070	56716.98 \pm 0.19	-2.81 \pm 0.49	-2.72 \pm 0.46	1.12 \pm 0.04	1.17 \pm 0.02	normal
LSQ14mc	0.057	56696.88 \pm 0.21	-3.62 \pm 0.26	...	0.95 \pm 0.04	...	normal
PTF14gnl	0.054	56956.29 \pm 0.41	-2.91 \pm 0.40	...	1.04 \pm 0.04	...	normal
LSQ13dsm	0.042	56670.15 \pm 0.26	-2.69 \pm 0.27	-2.59 \pm 0.11	0.88 \pm 0.04	0.94 \pm 0.02	normal
LSQ13ry	0.030	56395.38 \pm 0.18	-2.84 \pm 0.20	-2.91 \pm 0.09	0.86 \pm 0.04	0.93 \pm 0.02	normal
LSQ14age	0.081	56734.76 \pm 0.49	-0.68 \pm 0.53	...	1.12 \pm 0.05	...	normal
LSQ14q	0.067	56672.60 \pm 0.29	-2.21 \pm 0.31	...	0.94 \pm 0.04	...	normal
LSQ14ahm	0.050	56736.19 \pm 0.45	-2.29 \pm 0.47	...	1.23 \pm 0.04	...	normal
LSQ14foj	0.046	56939.65 \pm 0.25	-0.99 \pm 0.30	...	1.05 \pm 0.04	...	normal
LSQ14fom	0.056	56937.59 \pm 0.16	-2.25 \pm 0.24	...	0.92 \pm 0.04	...	normal
LSQ14gov	0.090	57027.74 \pm 0.18	-2.58 \pm 0.29	...	1.11 \pm 0.04	...	normal
LSQ14ie	0.090	56687.97 \pm 0.30	-2.09 \pm 0.50	...	1.22 \pm 0.04	...	normal
SN2005W	0.009	53411.33 \pm 0.25	-2.29 \pm 0.27	...	0.92 \pm 0.04	...	normal
LSQ14jp	0.045	56692.21 \pm 0.11	-0.49 \pm 0.13	...	0.64 \pm 0.04	...	normal
SN2007bd	0.031	54206.29 \pm 0.24	-3.53 \pm 0.31	-3.98 \pm 0.21	0.88 \pm 0.04	0.97 \pm 0.03	normal
LSQ13dpm	0.051	56656.91 \pm 0.15	-2.76 \pm 0.25	...	1.07 \pm 0.04	...	normal









Table A1
(Continued)

SN Name	Redshift	t_{\max}^B (MJD)	t_{\max}^{i-B} (days)	t_{\max}^{i-g} (days)	S_{BV}	S_{gr}	SN Type
SN2004eo	0.016	53278.24 \pm 0.11	-2.90 \pm 0.12	-3.50 \pm 0.08	0.82 \pm 0.04	0.87 \pm 0.01	normal
SN2004ey	0.016	53303.73 \pm 0.13	-2.98 \pm 0.16	-3.37 \pm 0.10	1.01 \pm 0.04	1.09 \pm 0.01	normal
SN2004gs	0.027	53355.92 \pm 0.13	-1.90 \pm 0.40	-2.28 \pm 0.38	0.70 \pm 0.04	0.74 \pm 0.01	normal
SN2005el	0.015	53647.02 \pm 0.45	-3.04 \pm 0.49	-2.86 \pm 0.20	0.84 \pm 0.04	0.87 \pm 0.01	normal
SN2005iq	0.034	53687.36 \pm 0.05	-3.14 \pm 0.12	-3.37 \pm 0.11	0.87 \pm 0.04	0.96 \pm 0.04	normal
SN2005kc	0.015	53697.61 \pm 0.16	-3.05 \pm 0.21	...	0.90 \pm 0.04	...	normal
SN2015F	0.005	57106.46 \pm 0.26	-2.47 \pm 0.31	-2.88 \pm 0.18	0.85 \pm 0.04	0.9 \pm 0.01	normal
SN2014I	0.030	56683.53 \pm 0.14	-2.65 \pm 0.17	-2.69 \pm 0.11	0.90 \pm 0.04	0.96 \pm 0.02	normal
SN2005ki	0.019	53704.75 \pm 0.14	-2.97 \pm 0.27	-3.67 \pm 0.24	0.83 \pm 0.04	0.86 \pm 0.01	normal
SN2014at	0.032	56774.07 \pm 0.17	-3.44 \pm 0.32	-3.29 \pm 0.27	0.93 \pm 0.04	1.02 \pm 0.02	normal
SN2013M	0.035	56323.28 \pm 0.28	-1.89 \pm 0.33	-2.00 \pm 0.20	0.93 \pm 0.04	0.96 \pm 0.02	normal
SN2013H	0.016	56309.43 \pm 0.18	-2.99 \pm 0.20	-3.34 \pm 0.11	1.06 \pm 0.04	1.12 \pm 0.01	normal
PTF14w	0.019	56669.55 \pm 0.17	-2.21 \pm 0.19	-2.59 \pm 0.10	0.73 \pm 0.04	0.75 \pm 0.01	normal
SN2013gy	0.014	56648.71 \pm 0.15	-2.89 \pm 0.16	-2.96 \pm 0.09	0.89 \pm 0.04	0.96 \pm 0.01	normal
SN2013E	0.009	56307.38 \pm 0.22	-2.54 \pm 0.24	-3.40 \pm 0.10	1.12 \pm 0.04	1.09 \pm 0.01	normal
SN2005M	0.022	53405.50 \pm 0.19	-2.93 \pm 0.21	-3.03 \pm 0.09	1.21 \pm 0.04	1.18 \pm 0.02	normal
SN2013aj	0.009	56361.45 \pm 0.27	-3.42 \pm 0.39	-3.46 \pm 0.28	0.78 \pm 0.04	0.83 \pm 0.01	normal
SN2013aa	0.004	56343.15 \pm 0.20	-3.63 \pm 0.34	-3.76 \pm 0.28	1.00 \pm 0.04	1.1 \pm 0.01	normal
SN2012ij	0.011	56302.33 \pm 0.10	-0.06 \pm 0.16	-0.54 \pm 0.13	0.53 \pm 0.04	0.6 \pm 0.01	normal
SN2012ht	0.004	56295.22 \pm 0.39	-1.81 \pm 0.42	-2.18 \pm 0.19	0.86 \pm 0.04	0.92 \pm 0.02	normal
SN2012hr	0.008	56288.72 \pm 0.22	-3.04 \pm 0.23	-3.28 \pm 0.09	0.96 \pm 0.04	1.02 \pm 0.01	normal
SN2012hd	0.012	56264.97 \pm 0.14	-2.44 \pm 0.18	-2.82 \pm 0.11	0.87 \pm 0.04	0.92 \pm 0.01	normal
SN2012gm	0.015	56261.79 \pm 0.08	-3.29 \pm 0.11	...	0.98 \pm 0.04	...	normal
SN2012fr	0.006	56242.28 \pm 0.34	-2.67 \pm 0.42	-2.91 \pm 0.26	1.12 \pm 0.04	1.19 \pm 0.01	normal
SN2011jh	0.008	55930.21 \pm 0.12	-2.16 \pm 0.13	-2.93 \pm 0.07	0.80 \pm 0.04	0.84 \pm 0.01	normal
PTF14yy	0.043	56732.58 \pm 0.19	-0.87 \pm 0.24	...	0.82 \pm 0.04	...	normal
SN2013fy	0.031	56600.55 \pm 0.22	-0.24 \pm 0.28	...	1.19 \pm 0.04	...	normal
SN2006gj	0.028	54000.06 \pm 0.22	-0.91 \pm 0.43	-1.44 \pm 0.38	0.66 \pm 0.04	0.88 \pm 0.07	normal
ASAS14jz	0.016	56980.56 \pm 0.08	-2.79 \pm 0.14	...	0.98 \pm 0.04	...	normal
ASAS14hu	0.022	56935.05 \pm 0.20	-2.60 \pm 0.29	-2.58 \pm 0.22	1.08 \pm 0.04	1.16 \pm 0.03	normal
ASAS14hr	0.034	56932.12 \pm 0.21	-1.03 \pm 0.29	-1.21 \pm 0.22	0.78 \pm 0.04	0.85 \pm 0.02	normal
ASAS14ad	0.026	56691.61 \pm 0.15	-2.12 \pm 0.18	-2.89 \pm 0.11	1.03 \pm 0.04	1.08 \pm 0.02	normal
SN2006gt	0.045	54003.00 \pm 0.20	-0.81 \pm 0.24	-1.23 \pm 0.15	0.56 \pm 0.04	0.68 \pm 0.03	normal
SN2006kf	0.021	54041.03 \pm 0.16	-2.43 \pm 0.19	-2.81 \pm 0.12	0.74 \pm 0.04	0.77 \pm 0.01	normal
SN2009Y	0.009	54875.37 \pm 0.20	-1.51 \pm 0.27	-2.57 \pm 0.20	1.19 \pm 0.04	1.02 \pm 0.01	normal
SN2009ds	0.019	54960.03 \pm 0.16	-1.90 \pm 0.33	...	1.13 \pm 0.05	...	normal
SN2009D	0.025	54840.61 \pm 0.32	-3.04 \pm 0.35	-3.20 \pm 0.15	1.19 \pm 0.04	1.16 \pm 0.03	normal
SN2009cz	0.021	54942.31 \pm 0.18	-2.82 \pm 0.22	...	1.19 \pm 0.04	...	normal
SN2009ad	0.028	54885.59 \pm 0.16	-2.87 \pm 0.18	...	1.02 \pm 0.04	...	normal
SN2009ab	0.011	54882.94 \pm 0.19	-3.15 \pm 0.20	...	0.87 \pm 0.04	...	normal
SN2007ca	0.014	54226.95 \pm 0.25	-2.94 \pm 0.33	...	1.06 \pm 0.04	...	normal
SN2007le	0.007	54398.40 \pm 0.36	-2.19 \pm 0.39	-2.80 \pm 0.16	1.03 \pm 0.04	1.05 \pm 0.01	normal
SN2007af	0.006	54174.07 \pm 0.24	-2.84 \pm 0.28	-3.12 \pm 0.14	0.93 \pm 0.04	1.0 \pm 0.01	normal
SN2007on	0.007	54420.16 \pm 0.09	-1.99 \pm 0.22	-2.03 \pm 0.20	0.57 \pm 0.04	0.62 \pm 0.01	normal
SN2008bf	0.024	54554.46 \pm 0.22	-3.74 \pm 0.28	-3.81 \pm 0.18	1.02 \pm 0.04	1.12 \pm 0.02	normal
SN2006ob	0.059	54062.95 \pm 0.20	-1.20 \pm 0.41	-1.69 \pm 0.36	0.72 \pm 0.04	0.79 \pm 0.03	normal
SN2008fp	0.006	54729.53 \pm 0.29	-2.25 \pm 0.31	-2.91 \pm 0.11	1.08 \pm 0.04	1.12 \pm 0.01	normal
SN2008gp	0.033	54778.82 \pm 0.24	-3.67 \pm 0.26	-3.74 \pm 0.13	0.97 \pm 0.04	1.03 \pm 0.08	normal
SN2008hj	0.038	54800.83 \pm 0.14	-2.79 \pm 0.19	...	1.01 \pm 0.04	...	normal
SN2008hv	0.013	54816.74 \pm 0.28	-3.53 \pm 0.30	-4.00 \pm 0.11	0.85 \pm 0.04	0.89 \pm 0.02	normal
SN2008bc	0.015	54548.83 \pm 0.17	-2.66 \pm 0.21	-3.28 \pm 0.13	1.05 \pm 0.04	1.08 \pm 0.01	normal
LSQ13dkp	0.069	56641.97 \pm 0.14	-1.71 \pm 0.29	...	0.63 \pm 0.04	...	normal
ASAS14me	0.018	57019.67 \pm 0.19	-2.92 \pm 0.20	-2.88 \pm 0.09	1.09 \pm 0.04	1.19 \pm 0.04	normal
LSQ13cwp	0.067	56611.57 \pm 0.32	-0.75 \pm 0.41	...	0.91 \pm 0.05	...	normal
LSQ13aiz	0.009	56437.25 \pm 0.14	-0.82 \pm 0.21	...	0.96 \pm 0.04	...	normal
LSQ12hzs	0.072	56298.56 \pm 0.16	-2.12 \pm 0.27	...	1.09 \pm 0.05	...	normal
LSQ12gxj	0.036	56274.88 \pm 0.17	-2.36 \pm 0.23	...	1.10 \pm 0.04	...	normal
SN2006ax	0.017	53827.11 \pm 0.25	-3.26 \pm 0.29	-3.06 \pm 0.16	0.99 \pm 0.04	1.07 \pm 0.02	normal
LSQ12fxd	0.031	56246.07 \pm 0.19	-2.52 \pm 0.31	...	1.10 \pm 0.04	...	normal
LSQ12fvl	0.056	56239.83 \pm 0.11	0.00 \pm 0.22	...	0.59 \pm 0.04	...	normal
LSQ12bld	0.083	56025.04 \pm 0.32	-2.09 \pm 0.36	...	0.85 \pm 0.04	...	normal
SN2006bh	0.011	53833.31 \pm 0.11	-3.59 \pm 0.23	-3.72 \pm 0.20	0.80 \pm 0.04	0.86 \pm 0.01	normal
SN2006D	0.009	53757.35 \pm 0.14	-2.56 \pm 0.19	-2.83 \pm 0.13	0.82 \pm 0.04	0.84 \pm 0.01	normal

Table A1
(Continued)

SN Name	Redshift	t_{\max}^B (MJD)	t_{\max}^{i-B} (days)	t_{\max}^{i-g} (days)	S_{BV}	S_{gr}	SN Type
KISS13v	0.080	56395.62 \pm 0.13	-0.23 \pm 0.31	...	1.03 \pm 0.05	...	normal
PSN 13-24 ^c	0.020	57069.77 \pm 0.21	-0.77 \pm 0.51	-1.14 \pm 0.47	0.71 \pm 0.04	0.76 \pm 0.02	normal
SN2006et	0.022	53993.16 \pm 0.14	-2.68 \pm 0.18	-2.98 \pm 0.12	1.09 \pm 0.04	1.15 \pm 0.02	normal
ASAS14mw	0.027	57028.20 \pm 0.18	-3.05 \pm 0.42	-3.83 \pm 0.38	1.07 \pm 0.04	1.11 \pm 0.01	normal
ASAS14my	0.021	57029.99 \pm 0.27	-2.08 \pm 0.30	-2.82 \pm 0.16	0.91 \pm 0.04	0.98 \pm 0.02	normal
ASAS15be	0.022	57048.59 \pm 0.29	-1.42 \pm 0.44	-2.23 \pm 0.34	1.20 \pm 0.04	1.14 \pm 0.01	normal
ASAS15bm	0.021	57053.21 \pm 0.31	-2.26 \pm 0.37	-3.11 \pm 0.22	0.99 \pm 0.04	1.11 \pm 0.08	normal
ASAS14lw	0.021	57012.25 \pm 0.40	-2.26 \pm 0.41	...	1.26 \pm 0.04	...	normal
CSS120305 ^d	0.097	56022.06 \pm 0.20	-2.42 \pm 0.34	...	1.11 \pm 0.04	...	normal
CSS130303 ^e	0.079	56364.02 \pm 0.38	-1.57 \pm 0.43	...	1.19 \pm 0.04	...	normal
OGLE14-019 ^f	0.036	56718.28 \pm 0.25	-2.06 \pm 0.34	-1.67 \pm 0.28	0.89 \pm 0.04	1.12 \pm 0.03	normal
ASAS15hf	0.006	57136.89 \pm 0.13	-2.67 \pm 0.23	-3.26 \pm 0.19	0.92 \pm 0.04	0.89 \pm 0.01	normal
SN2004ef	0.031	53263.77 \pm 0.12	-3.32 \pm 0.12	-3.70 \pm 0.04	0.82 \pm 0.04	0.83 \pm 0.01	normal

Notes.^a SN full name: MLS140102:120307-010132^b This lower limit was calculated using the sBV vs $\Delta m_{15}(B)$ relation for the 03fg-like SNe^c SN full name: PSN J13471211-2422171.^d SN full name: CSS120325:123816-150632.^e SN full name: CSS130303:105206-133424.^f SN full name: OGLE-2014-SN-019.**ORCID iDs**

C. Ashall  <https://orcid.org/0000-0002-5221-7557>
E. Y. Hsiao  <https://orcid.org/0000-0003-1039-2928>
M. Stritzinger  <https://orcid.org/0000-0002-5571-1833>
E. Baron  <https://orcid.org/0000-0001-5393-1608>
L. Galbany  <https://orcid.org/0000-0002-1296-6887>
P. Hoefflich  <https://orcid.org/0000-0002-4338-6586>
N. Morrell  <https://orcid.org/0000-0003-2535-3091>
E. Karamahmetoglu  <https://orcid.org/0000-0001-6209-838X>
K. Krisciunas  <https://orcid.org/0000-0002-6650-694X>

References

- Ashall, C., Hoefflich, P., Hsiao, E. Y., et al. 2019a, *ApJ*, **878**, 86
Ashall, C., Hsiao, E. Y., Hoefflich, P., et al. 2019b, *ApJL*, **875**, L14
Ashall, C., Mazzali, P. A., Stritzinger, M. D., et al. 2018, *MNRAS*, **477**, 153
Betoule, M., Kessler, R., Guy, J., et al. 2014, *A&A*, **568**, A22
Branch, D., Dang, L. C., Hall, N., et al. 2006, *PASP*, **118**, 560
Burns, C. R., Parent, E., Phillips, M. M., et al. 2018, *ApJ*, **869**, 56
Burns, C. R., Stritzinger, M., Phillips, M. M., et al. 2011, *AJ*, **141**, 19
Burns, C. R., Stritzinger, M., Phillips, M. M., et al. 2014, *ApJ*, **789**, 32
Chen, P., Dong, S., Katz, B., et al. 2019, *ApJ*, **880**, 35
Contreras, C., Hamuy, M., Phillips, M. M., et al. 2010, *AJ*, **139**, 519
Feindt, U., Kerschhaggl, M., Kowalski, M., et al. 2015, *A&A*, **578**, C1
Filippenko, A. V., Richmond, M. W., Branch, D., et al. 1992a, *AJ*, **104**, 1543
Filippenko, A. V., Richmond, M. W., Matheson, T., et al. 1992b, *ApJL*, **384**, L15
Foley, R. J., Challis, P. J., Chornock, R., et al. 2013, *ApJ*, **767**, 57
Foley, R. J., Narayan, G., Challis, P. J., et al. 2010, *ApJ*, **708**, 1748
Galbany, L., Ashall, C., Hoefflich, P., et al. 2019, *A&A*, **630**, A76
González-Gaitán, S., Hsiao, E. Y., Pignata, G., et al. 2014, *ApJ*, **795**, 142
Hachinger, S., Mazzali, P. A., Taubenberger, S., et al. 2012, *MNRAS*, **427**, 2057
Hamuy, M., Phillips, M. M., Suntzeff, N. B., et al. 2003, *Natur*, **424**, 651
Hicken, M., Garnavich, P. M., Prieto, J. L., et al. 2007, *ApJL*, **669**, L17
Hoefflich, P., & Khokhlov, A. 1996, *ApJ*, **457**, 500
Höflich, P., Gerardy, C. L., Fesen, R. A., et al. 2002, *ApJ*, **568**, 791
Howell, D. A., Sullivan, M., Nugent, P. E., et al. 2006, *Natur*, **443**, 308
Hsiao, E. Y., Burns, C. R., Contreras, C., et al. 2015, *A&A*, **578**, A9
Hsiao, E. Y., Phillips, M. M., Marion, G. H., et al. 2019, *PASP*, **131**, 014002
Jack, D., Baron, E., & Hauschildt, P. H. 2015, *MNRAS*, **449**, 3581
Jha, S. W. 2017, in *Handbook of Supernovae*, ed. A. Alsabti & P. Murdin (Berlin: Springer), 375
Kasen, D. 2006, *ApJ*, **649**, 939
Krisciunas, K., Contreras, C., Burns, C. R., et al. 2017, *AJ*, **154**, 211
Leibundgut, B., Kirshner, R. P., Phillips, M. M., et al. 1993, *AJ*, **105**, 301
Li, W., Filippenko, A. V., Chornock, R., et al. 2003, *PASP*, **115**, 453
Nugent, P., Phillips, M., Baron, E., et al. 1995, *ApJL*, **455**, L147
Perlmutter, S., Aldering, G., Goldhaber, G., et al. 1999, *ApJ*, **517**, 565
Phillips, M. M., Li, W., Frieman, J. A., et al. 2007, *PASP*, **119**, 360
Phillips, M. M., Wells, L. A., Suntzeff, N. B., et al. 1992, *AJ*, **103**, 1632
Phillips, M. M., Contreras, C., Hsiao, E. Y., et al. 2019, *PASP*, **131**, 014001
Prentice, S. J., Ashall, C., Mazzali, P. A., et al. 2018, *MNRAS*, **478**, 4162
Riess, A. G., Filippenko, A. V., Challis, P., et al. 1998, *AJ*, **116**, 1009
Saselli, M., Mazzali, P. A., Pian, E., et al. 2014, *MNRAS*, **445**, 711
Scalzo, R. A., Aldering, G., Antilogus, P., et al. 2010, *ApJ*, **713**, 1073
Schlafly, E. F., & Finkbeiner, D. P. 2011, *ApJ*, **737**, 103
Schmidt, B. P., Kirshner, R. P., Eastman, R. G., et al. 1993, *Natur*, **364**, 600
Scolnic, D. M., Jones, D. O., Rest, A., et al. 2018, *ApJ*, **859**, 101
Stritzinger, M., Phillips, M. M., Contreras, C., et al. 2011, *AJ*, **142**, 156
Stritzinger, M. D., Valenti, S., Hoefflich, P., et al. 2015, *A&A*, **573**, A2
Taddia, F., Stritzinger, M. D., Bersten, M., et al. 2018, *A&A*, **609**, A136
Taubenberger, S., Benetti, S., Childress, M., et al. 2011, *MNRAS*, **412**, 2735
Taubenberger, S., Floers, A., Vogl, C., et al. 2019, *MNRAS*, **488**, 5473
Valenti, S., Fraser, M., Benetti, S., et al. 2011, *MNRAS*, **416**, 3138
Wheeler, J. C., Höflich, P., Harkness, R. P., et al. 1998, *ApJ*, **496**, 908